COMPUTER METHODS AND PROGRAMS IN BIOMEDICINE 108 (2012) 186–196

journal homepage: www.intl.elsevierhealth.com/journals/cmpb

An automated decision-support system for non-proliferative diabetic retinopathy disease based on MAs and HAs detection

Marwan D. Saleh, C. Eswaran*

Centre for Visual Computing, Faculty of Computing and Informatics, Multimedia University, Jalan Multimedia, 63100 Cyberjaya, Selangor, Malaysia

ARTICLE INFO

Article history:
Received 24 March 2011
Received in revised form
6 March 2012
Accepted 12 March 2012

Keywords:
Diabetic retinopathy
Dark spots segmentation
Dark spots classification
Centroid distance method
Contrast enhancement
h-Maxima transform
Multilevel thresholding
Mathematical morphology

ABSTRACT

Diabetic retinopathy (DR) has become a serious threat in our society, which causes 45% of the legal blindness in diabetes patients. Early detection as well as the periodic screening of DR helps in reducing the progress of this disease and in preventing the subsequent loss of visual capability. This paper provides an automated diagnosis system for DR integrated with a user-friendly interface. The grading of the severity level of DR is based on detecting and analyzing the early clinical signs associated with the disease, such as microaneurysms (MAs) and hemorrhages (HAs). The system extracts some retinal features, such as optic disc, fovea, and retinal tissue for easier segmentation of dark spot lesions in the fundus images. That is followed by the classification of the correctly segmented spots into MAs and HAs. Based on the number and location of MAs and HAs, the system quantifies the severity level of DR. A database of 98 color images is used in order to evaluate the performance of the developed system. From the experimental results, it is found that the proposed system achieves 84.31% and 87.53% values in terms of sensitivity for the detection of MAs and HAs respectively. In terms of specificity, the system achieves 93.63% and 95.08% values for the detection of MAs and HAs respectively. Also, the proposed system achieves 68.98% and 74.91% values in terms of kappa coefficient for the detection of MAs and HAs respectively. Moreover, the system yields sensitivity and specificity values of 89.47% and 95.65% for the classification of DR versus normal.

1. Introduction

Diabetic retinopathy (DR) is one of the well-known and commonest eye diseases, affecting patients with diabetes mellitus. DR is potentially considered as the major reason behind blindness in adults of age between 20 and 60 years, where it causes 45% of the legal blindness in patients with Diabetes Mellitus [1]. Moreover, DR has become a serious threat in our society, where the number of patients with DR is considerably increasing as a result of the increasing number of people affected by diabetes mellitus. According to Lee et al. [2], blindness due to diabetic eye disease costs about 500 million dollars a year in the United States [3]. As DR is a progressive disease, the longer a patient has untreated diabetes, the higher his chance of progress towards blindness [4]. For this reason, early detection as well as the periodic screening of DR potentially helps in reducing the progression of this disease and in preventing the subsequent loss of visual capability. Normally the screening should be done every 12 months (for severe cases

* *Corresponding author*. Tel.: +60 173110027.
E-mail addresses: marwan@mmu.edu.my (M.D. Saleh), eswaran@mmu.edu.my (C. Eswaran).
0169-2607/$ – see front matter © 2012 Elsevier Ireland Ltd. All rights reserved.
doi:10.1016/j.cmpb.2012.03.004

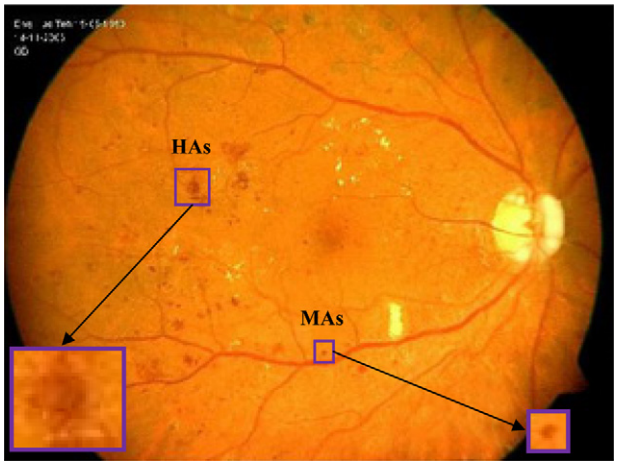

Fig. 1 – RGB retinal image acquired from one of the DR patients.

every 3 months), which includes obtaining and analyzing a sequence of fundus images and observing the early changes in blood vessel patterns and also the presence of the dark spots, such as microaneurysms (MAs) and hemorrhages (HAs). It is known that there exists a positive correlation between the number and location of MAs and HAs and the severity and progression of DR [5–8]. MAs are considered as the earliest observable signs indicating diabetic retinopathy. Besides, HAs also play an important role in the early detection of DR. MAs appear as small, round, and dark reddish spots with a diameter less than 125 μm. The smaller size as well as the background intensity variation makes the detection of MAs a complicated and problematic task. HAs are also reddish in color similar to MAs but they are larger in size and arbitrary shaped [9], as can be seen in Fig. 1.

In the literature, a number of methods have been reported to address the problem of MA and HA detection. The researchers in [10–13] have proposed mathematical morphology based methods for the detection of red spots. In [14], a hybrid method, combining prior works reported in [12,13] have been reported. In that paper, a system for the detection of red lesion candidate based on supervised pixel classification in addition to the employment of *k*-nearest neighbor classifier was developed. In fact, the method tends to be similar to the work reported in [15,16]. Walter et al. [17] have developed the last two methods to presents MA detection method, based on diameter closing and kernel density estimation for automatic classification. Neural network based methods have been proposed in [18–20] for the detection red spots. Another method has been proposed by Fleming et al. [21], which make use of the contrast normalization to overcome the lighting variations around candidate spot lesions, and eliminate the spots located on the blood vessels using the local vessel segmentation. The work in [22] presents a method for MA detection, based on template-matching with a generalized Gaussian template, and the template matching is performed in the wavelet domain.

This paper proposes a development of an automated decision-support system for DR disease based on the number and location of MAs and HAs. The system starts with the segmentation of MAs and HAs, followed by the classification of these spots. Based on the number of MAs and HAs, the system quantifies the severity level of DR. The proposed segmentation algorithm is based on a number of morphological operations [23,24], such as dilation, erosion, opening, closing, reconstructions, and top- and bottom-hat. The main components of the human retina are the optic disc, fovea, tissue and blood vessels. Removing these components will help in avoiding the false positives as much as possible. A powerful technique is proposed for detecting and removing the optic disc from the image, as will be explained later. As the retinal images are poorly contrasted, an effective combination of top- and bottom-hat is utilized for enhancing the image contrast. Furthermore, other techniques such as *h*-maxima transform [23] and multilevel thresholding [25] are exploited to decrease the intensity levels, and consequently, make the dark spots segmentation problem easier. An efficient dark spots classification algorithm will be described in Section 2, which is based on some geometrical criteria. Furthermore, a user-friendly interface is designed in order to enable the user to interact with the developed system.

2. Developed system

In this work, an automated decision-support system for non-proliferative DR disease is presented. Input to the developed system is a color image of human retina, which is acquired by using a fundus camera, and its outputs are binary images depicting the presence of spot lesions (MAs and/or HAs), and also displaying the severity level of DR. Fig. 2 shows the block diagram of the developed system.

A database of 98 low-resolution color images compressed by JPEG format was used in this work to test the accuracy of the proposed algorithms for dark spots segmentation and classification. The test images were collected by the University Malaya Medical Centre (UMMC), which were acquired from patients in different stages of DR. Our database comprises two sets of images with different resolutions. 62 images of size 480×640 pixels were acquired using a TopCon TRC-NW7SF Mydriatic/Non-Mydriatic Dual type retinal camera at 50° FOV. The remaining 36 images were of size 576×768 pixels and acquired using the same camera but at 45° FOV. The presence of MAs and HAs was manually marked by a specialist in the test images, and a comparison between the results of our algorithm against the hand-labeled images was done accordingly.

2.1. *Preprocessing*

Pre-processing is a crucial stage for preparing the fundus image for segmentation since image quality varies according to the conditions of acquisition. For instance, the image could be acquired under some undesired conditions, such as unevenly illuminated, noisy or low-contrasted images, which obviously influence the performance of segmentation algorithm. Hence the acquired RGB image has to undergo a sequence of preprocessing steps, which are green-channel extraction, optic disc removal, and background normalization.

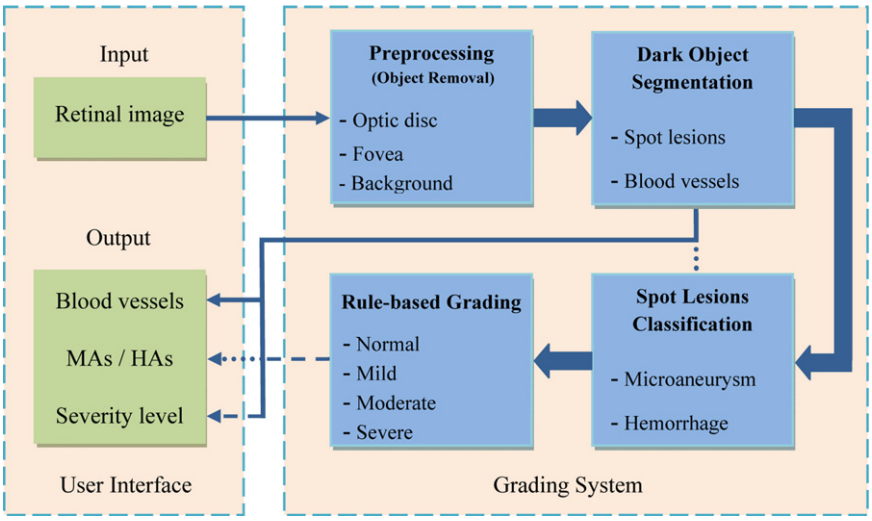

Fig. 2 – Block diagram of the developed decision-support system for DR disease.

2.1.1. *Green-channel extraction*

Color test images, as mentioned earlier, are divided into two sets based on size. The algorithm thus starts with resizing all input images to 600 × 800 pixels. Amongst the color image components (i.e. red, green, and blue), green-channel provides maximum local contrast among the image pixel values. As MAs and HAs are clearly distinct from the other retinal features, the green-channel I_G is first extracted from the RGB image. Whilst the total number of levels possible for a color image is about 16 million (2^{24}) levels, the green image contains only 256 levels. Thus, such conversion will decrease the computational time, as well as the storage space.

2.1.2. *Optic disc removal*

Pre-processing stage includes removing some retinal features, namely optic disc and fovea from the retinal image. Fovea, which appears as a dark region and located in the center of retina, will be excluded for the subsequent steps. Optic disc (OD) in general has some characteristics, such as high intensity, circular shape, and constant size which indicate its exact location in the image. Normally, some dark objects could appear inside the optic disc which may be incorrectly considered as MAs or HAs. Hence optic disc removal helps to eliminate those confusing objects.

Clearly, optic disc is located in the middle third of the image due to the position of the imaging device. For this reason, the proposed method for optic disc removal starts with focusing on the middle third of the green intensity image f_G as a region of interest (ROI), as can be seen in Fig. 3(a). Next, the image is processed with a median filter of size 11 × 11 pixels to fill up the thin blood vessel regions inside OD. The resulting image after applying median filter is shown in Fig. 3(b). Unlike the neighborhood averaging filter (mean filter), the median filter can perform this task without blurring the border sharp edges,

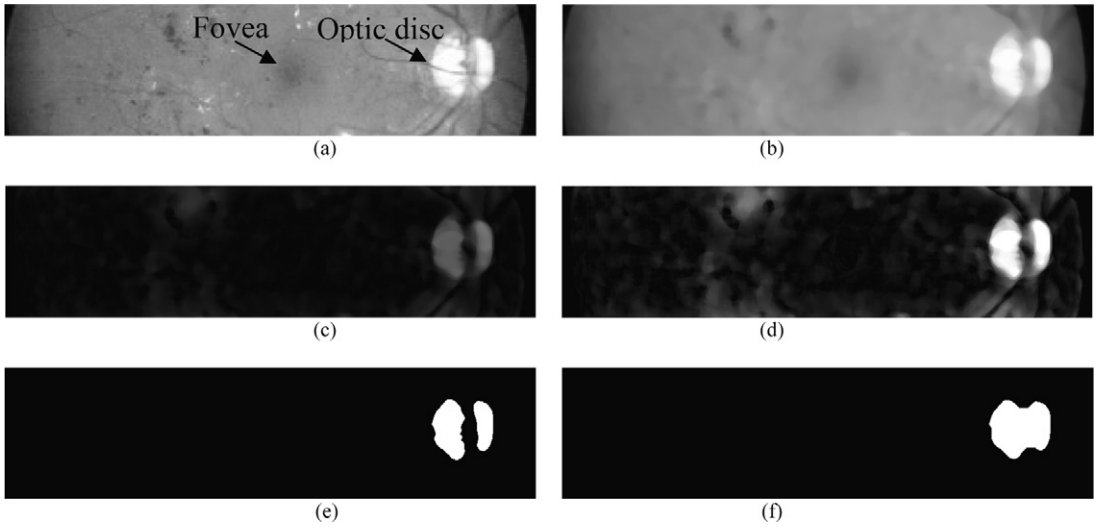

Fig. 3 – Illustration of optic disc removal steps (a) green intensity image (b) median-filtered image (c) contrast-enhanced image (d) contrast-stretched image (e) binary image (f) rough location of the optic disc.

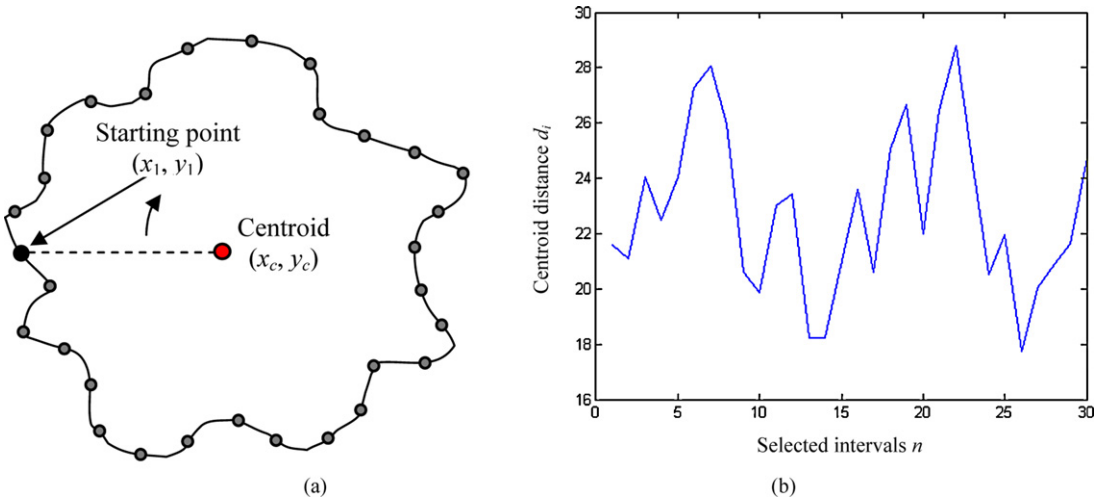

Fig. 4 – Explanatory illustration of CDM (a) centroid distance function, (b) feature vector of (a).

i.e. the borders of the OD or retina. Basically, the median filter replaces the value of the pixel $f_G(x, y)$ by the median of all pixels in the neighborhood of this pixel, as follows:

$$f_{med}(x, y) = \underset{(s,t) \in W_{xy}}{\text{median}}\{f_G(s, t)\} \quad (1)$$

where W represents a neighborhood centered around location (x, y) in the image. The contrast of the resulting image f_{med} is then enhanced based on a morphological top-hat transform. The top-hat operation involves subtracting the result of performing a morphological opening on the input image f_{med} from the image itself based on a given structuring element SE, as in Eq. (2):

$$T(f_{med}) = f_{med} - (f_{med} \circ SE) \quad (2)$$

In our implementation, the contrast has been enhanced using a ball structuring element with a radius of size 60 pixels, where the size of the structuring element has to be large enough to contain the optic disc region. The resulting image after top-hat operation is illustrated in Fig. 3(c). As the resulting image $T(f_{med})$ is low contrasted, contrast stretching is then used to obtain an image f_{CS} by expanding the range of intensity values of the contrast-enhanced image so that the full dynamic range of the image is covered. This process can be performed by specifying lower and upper limits that can be used for contrast stretching So that data is saturated at low and high intensities of image T. Values of lower and upper limits used in the proposed algorithm specify the bottom 1% and the top 1% of all pixel values [25]. The resulting image f_{CS} is shown in Fig. 3(d). The green intensity image f_{CS} is then converted to a binary image f_{BW} using a threshold value $T = \max(f_{CS}) - 10$, as follows:

$$f_{BW}(x, y) \begin{cases} 1 & \text{if } f_{cs}(x, y) \geq \\ 0 & \text{Otherwise} \end{cases} \quad (3)$$

The resulting image after thresholding is shown in Fig. 3(e). In order to detect the rough location of the optic disc, both morphological opening and closing operations are utilized. Morphological opening is utilized for eliminating small objects, which are not likely to be the OD. This is followed by closing operation to conglutinate the adjacent objects using a flat structuring element of size 15×15 pixels. The resulting image is shown in Fig. 3(f).

At the end of these steps, only one object may remain in most of the cases, which represents the optic disc. However, the image sometimes contains bright spot lesion(s) (i.e. cotton–wool), which may be similar to the optic disc in terms of size and intensity level. In such cases, a subsequent method is proposed in this work to specify the accurate location of the optic disc based on the shape. The proposed method is inspired from the so-called *Centroid Distance Method* (CDM). The method is implemented by dividing the candidate region boundary into *n* equally spaced intervals (points), which efficiently specify the boundary feature. Then, the location of the centroid point (x_c, y_c) is obtained using Eq. (4); for each candidate region, the centroid distance function (*d*), which is defined as the distance of the selected outline boundary points (x_i, y_i) to the centroid (x_c, y_c) of the region is then calculated using Eq. (5). Among the contour points, the point with orientation 0° from the centroid is selected as the starting point. Afterwards, distance values are arranged into a one-dimensional array, called feature vector *F*, as illustrated in Fig. 4.

$$x_c = \frac{1}{N}\sum_{i=0}^{N-1} x_i, \; y_c = \frac{1}{N}\sum_{i=0}^{N-1} y_i \quad (4)$$

$$d_i = \left| \sqrt{(x_i - x_c)^2 + (y_i - y_c)^2} \right| \quad i = 1, \ldots, n \quad (5)$$

Logically, the region which has a feature vector with smallest standard deviation σ_k is calculated using Eq. (6) among

Fig. 5 – Optic disc removal.

the candidates will be the closest region to circularity, and consequently represent the optic disc.

$$\sigma_k(F) = \frac{1}{n}\sqrt{\sum_{i=1}^{n}(F_k(i) - \mu_k(F))^2}, \quad k = 1 \ldots \text{no. of candidates} \quad (6)$$

In Eq. (6), μ represents the mean value of the feature vector. After determining the accurate location of OD, a circular-shaped mask of radius equal to 50 pixels is cross-correlated with the OD region to remove the OD disc region. Fig. 5 shows the resulting green intensity image I_G after optic disc removal.

2.1.3. *Background removal*

The background removal process aims at eliminating background variations in illumination from an image so that the foreground objects may be more easily analyzed, which will represent the brighter part in the image. It is necessary to deepen the contrast of images first to provide a better transform representation for subsequent image analysis steps. Low-contrasted images may occur due to several reasons, such as poor or non-uniform lighting condition, nonlinearity or small dynamic range of the imaging sensor, i.e. illumination is distributed non-uniformly within that image.

A wide variety of techniques can be employed to enhance the image contrast, such as top-hat transform, bottom-hat transform, decorrelation stretch transform, histogram equalization (HE), adaptive histogram equalization (AHE), contrast-limited adaptive histogram equalization (CLAHE), etc. In the proposed algorithm, both morphological top- and bottom-hat transforms are exploited to perform the contrast enhancement. The combination of top- and bottom-hat is used here for getting good prominence for the dark spot lesions with minimal effect on the background intensity levels. As indicated previously, top-hat operation involves subtracting the result of performing a morphological opening on an image I_G from the image itself. On the contrary, bottom-hat operation is performed by subtracting the image I_G from the result of performing a morphological closing on the input image. Generally, the effect of the top- and bottom-hat operations are based on a predefined neighborhood or structuring element *SE*, as illustrated in Eqs. (7) and (8) respectively:

$$T_{hat}(I_G) = I_G - (I_G \circ SE) \quad (7)$$

$$B_{hat}(I_G) = (I_G \bullet SE) - I_G \quad (8)$$

Using a 5×5 flat structuring element, the proposed algorithm enhances the contrast of the image based on the following formula:

$$I_{CE} = (I_G + I_{hat}(I_G)) - B_{hat}(I_G) \quad (9)$$

where I_{CE} represents a contrast-enhanced intensity image. The result of using the combination of top- and bottom-hat transformations on the image of Fig. 5 is shown in Fig. 6(a) in the next step, image background is removed using Eq. (10), by subtracting the contrast-enhanced image I_{CE} from the median-filtered image I_{med}, with 25×25 pixels which is shown in Fig. 6(b). Mathematically, the difference image I_{BN} between two images I_{med} and I_{CE}, is generated by computing the difference 't' between all pairs of corresponding pixels in $I_{med}(x, y)$ and $I_{CE}(x, y)$ [24], as shown in Eq. (10).

$$I_{BN}(x, y) = \begin{cases} t & \text{if } I_{med}(x, y) - I_{CE}(x, y) > 0 \\ 0 & \text{Otherwise} \end{cases} \quad (10)$$

Fig. 6(c) shows the resulting image I_{BN}. As the resulting image I_{BN} is low contrasted, contrast stretching is then used to obtain an image I_{CS} by expanding the range of intensity values of I_{BN} so that the full dynamic range of the image is covered, as shown in Fig. 6(c). In order to reduce the resulting noise in image I_{CS}, median filter is used once again but with a size of 5×5 pixels. Fig. 6(d) shows the resulting image I from the pre-processing stage.

2.2. *Dark spot segmentation*

In the proposed system, dark spot lesions, namely MAs and HAs, are segmented efficiently using a sequence of stages, which are: *h*-maxima transformation, thresholding and eventually, feature extraction.

2.2.1. *h-Maxima transformation*

In this stage, the resulting image from the pre-processing stage is processed by the *h*-maxima transform for reducing the number of intensity levels, which will be helpful in the subsequent stages. Let I be an intensity image; then the *h*-maxima transform is used for suppressing all maxima in the intensity image I whose values are less than a certain threshold h, as follows:

$$H_h(I) = R_I^{\delta}(I - h) \quad (11)$$

where R_I^{δ} describes the morphological reconstruction by dilation of image I. In general, images vary in the quality depending on the acquiring conditions. The image could be acquired under some undesired conditions, such as unevenly distributed gray intensities, which increases the difficulty of choosing a threshold value h. By trial and error, we found that

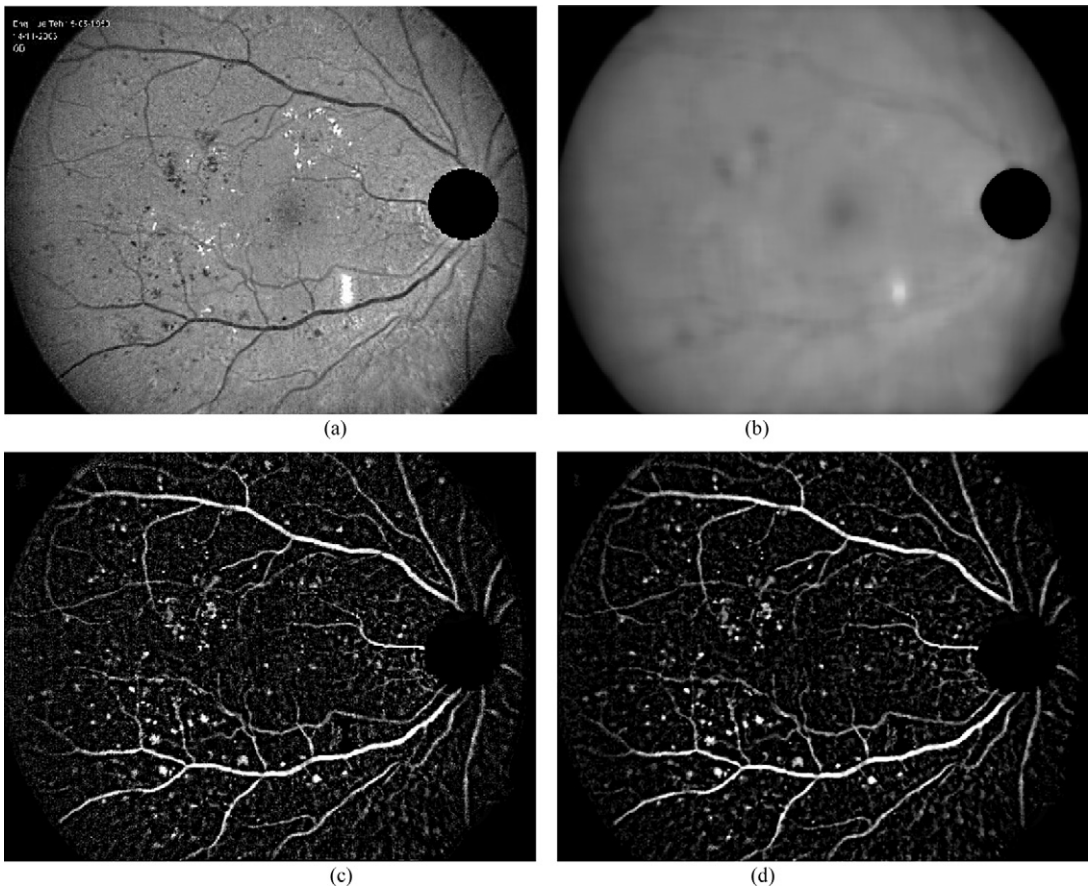

Fig. 6 – (a) Contrast-enhanced image with *SE* = 5 × 5 pixels (b) median-filtered image with 25 × 25 pixels (c) resulting image of subtracting (a) from (b), (d) median-filtered image with 5 × 5 pixels.

h can be selected based on an empirical formula shown in Eq. (12) to obtain the best accuracy values.

$$h = \frac{2}{N \times M} \sqrt{\sum_{i=1}^{N \times M} (I_i - \mu_I)^2} \tag{12}$$

where $N \times M$, μ denote the size, and mean value of image I respectively. Fig. 7(a) shows the resulting image after applying h-maxima transform to Fig. 6(d).

2.2.2. *Thresholding*

In this stage, both MAs and HAs are segmented by thresholding the intensity image H_h. Thresholding is one of the most commonly used methods in image segmentation, which aims here to produce a binary image in which the value of each pixel is either 1 (dark spot) or 0 (background). Unfortunately, there is no unique technique for thresholding which provides perfect results for all images. However, in the proposed algorithm, multilevel thresholding technique [25] is used to implement the binarization process efficiently. Simply, before converting to black and white, the image undergoes a multilevel thresholding process so that the threshold value can be selected easily. Multilevel thresholding converts the gray-scale image to an indexed image by decreasing the number of intensity levels. This is performed by separating the pixels of an intensity image into N groups $G_1 \ldots G_N$, based on a certain number of threshold values T_i, as follows:

$$T_i = \frac{i}{N-1}, \frac{i+1}{N-1}, \ldots, \frac{N-2}{N-1} \quad i = 1, \ldots, N-1 \tag{13}$$

Threshold values T_i can be obtained by analyzing the image histogram. Let S denote an intensity image. Each pixel (x, y) is assumed to belong to G_i if $T_{i-1} < S(x, y) \leq T_i$. In our implementation, the intensity levels are decreased to 4 levels to produce an image H_T in which the threshold value can be selected easily for binarization. Fig. 7(c) shows the histogram of Fig. 7(a). Fig. 7(c) and (d) shows the resulting image H_T and its histogram respectively.

From Fig. 7(d), it can be concluded that the threshold value T used for binarization can be selected in the range 30–180, (e.g. $T = 100$). Based on the threshold value T, a binary image H_{BW} can be obtained by thresholding the indexed image H_T, as follows:

$$H_{BW}(x, y) = \begin{cases} 1 & \text{if } H_T(x, y) \geq T \\ 0 & \text{Otherwise} \end{cases} \tag{14}$$

2.2.3. *Feature extraction*

As a result of the thresholding, blood vessels as well as some unwanted pixels will appear as false positive in the resultant binary image, and therefore, some post-processing should

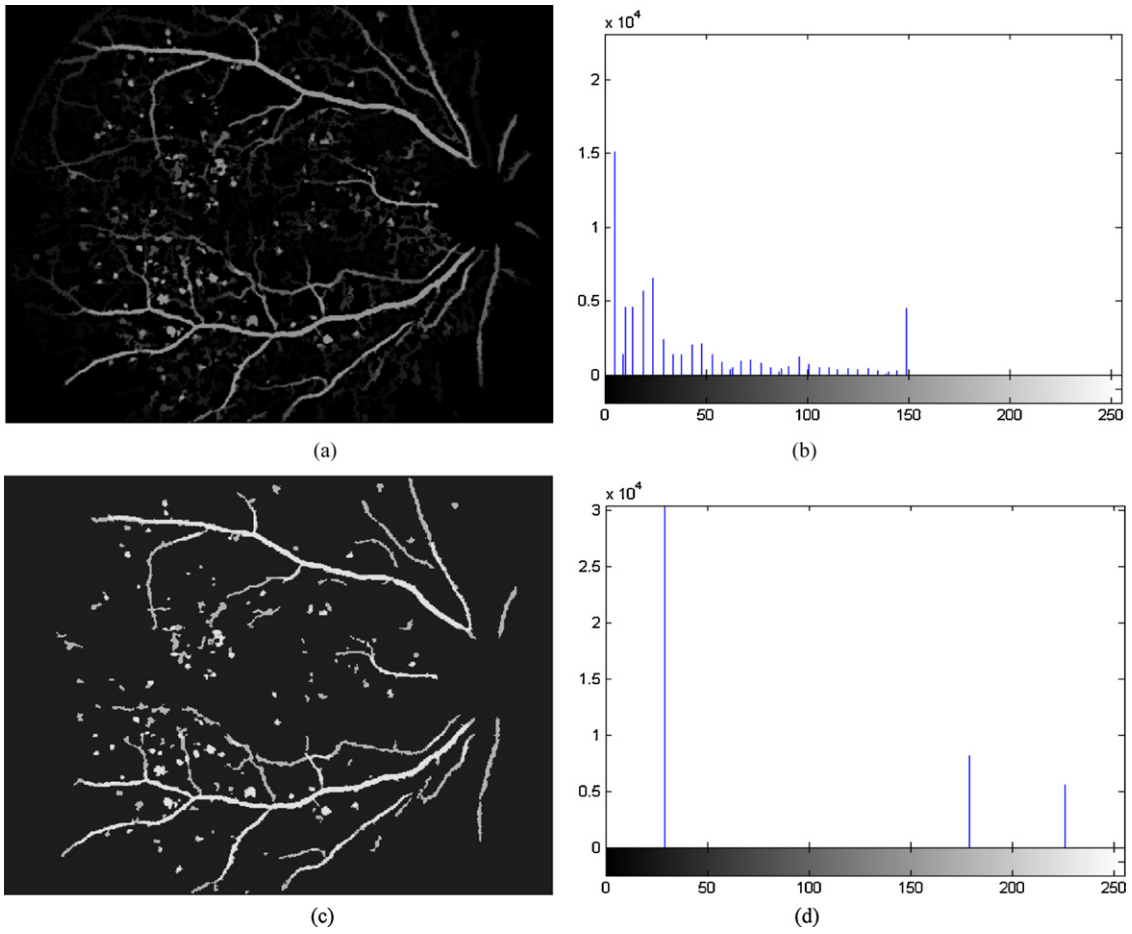

Fig. 7 – (a) *h*-Maxima transformed image (b) histogram of (a), (c) indexed image contains only four levels (d) histogram of (d).

be adopted for refining the image and retaining the desired objects, namely MAs and HAs. This process is implemented based on some geometrical criteria, namely density (*Den*), major axis (*Maj*) and minor axis (*Min*), as illustrated in Fig. 8. This is performed by labeling all the objects in the binary image, and calculating the object density and the ratio of major to minor axes for each one, as follows:

$$Den_i = \frac{Ar_i}{n_i} \quad i = 1 \ldots N \tag{15}$$

$$R_i = Maj_i/Min_i \quad i = 1 \ldots N \tag{16}$$

where Ar, n, Maj, Min and N represent the object area, bounding box area of the object, major axis, minor axis and the number of objects respectively.

Based on some suitable threshold values for Den and R, blood vessels and other unwanted objects can be excluded from the image H_{BW} and obtain an image H_S which contains only dark spots, viz. MAs and HAs, as can be seen in Fig. 9(b).

2.3. *Dark spot classification*

According to the Early Treatment Diabetic Retinopathy Study (ETDRS) [9,26], classification of the different spot lesions (i.e.

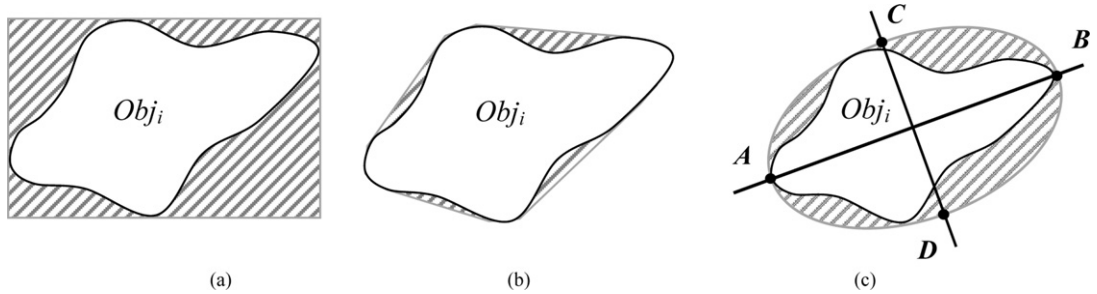

Fig. 8 – Illustration of geometric-based criteria (a) an object *Obj* and its bounding box (b) an object *Obj* and its convex region (c) major axis *AB* and minor axis *CD* of an object *Obj*.

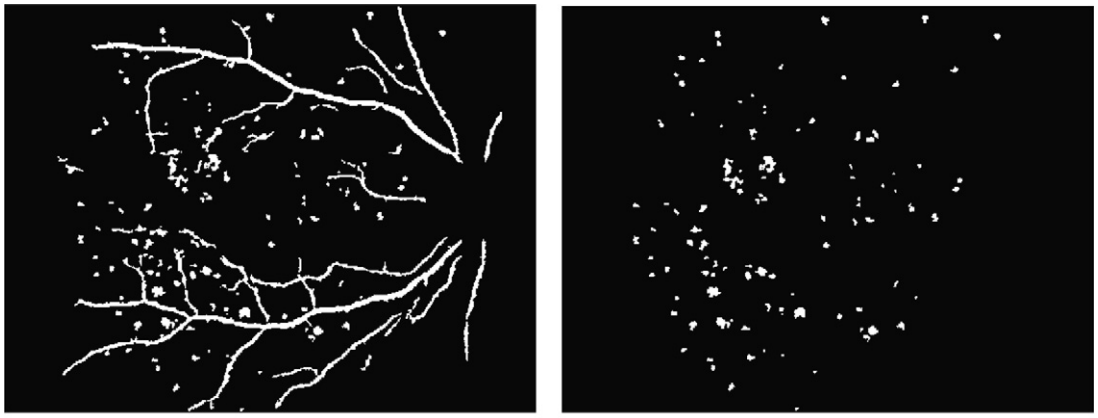

(a) (b)

Fig. 9 – (a) The resulting binary image with $T = 100$ (b) The result of dark spots segmentation stage.

cotton-wool spots, hard exudates, drusen, microaneurysms, hemorrhages) can be performed based on seven features, which are: size, shape, roughness, edge sharpness, brightness, color, and depth. In the current work, we are interested in the classification of MAs and HAs. Among the features above, MAs and HAs are similar with respect to five features, which are dull (roughness), insignificant edge (edge sharpness), dark (brightness), reddish (color), and superficial (depth). Hence the classification is mainly based on the remaining two features, i.e. size and shape.

In this work, some straightforward geometric-based criteria are used to classify MAs and HAs. As indicated earlier in the introduction, MAs appear as small and round spots, and therefore, size can be considered as the more significant evidence for classification. Based on some thresholds for the size, an object can be judged more likely whether it resemble MA or HA. In addition to the size, some other strict conditions can also be applied for an accurate classification. The converging values of major- and minor-axes of each object can be used as indicators for differentiating MAs and HAs. Furthermore, the ratio of an object area to its convex area (i.e. the area of a region which can be obtained under the smallest convex polygon) can also be exploited as evidence for the classification, as illustrated in Fig. 8(b). Fig. 10 shows two images which represent the output of the proposed classification algorithm. Fig. 10(a) shows the HAs and Fig. 10(b) shows the MAs.

2.4. *Severity level grading*

The various retinopathy severity scales presented in ETDRS [27] can be summarized in Table 1.In this work, the severity level of the Non-Proliferative DR (NPDR) is classified into several groups based on presence of MAs and HAs [28]. The severity levels described in Table 2 includes four scales of the disease with increasing risks of retinopathy. The first level is "no apparent retinopathy" (normal) includes ETDRS grade 10 which indicates no abnormality within the retina. The second level, "mild NPDR" includes ETDRS grade 20 which indicates the presence of MAs only in the retina. In these two groups (i.e. normal and mild NPDR), the risk of significant progression over several years is very low. The third level, "moderate NPDR," includes eyes with ETDRS grades 35–47 and the risk of progression increases significantly by level 47. Finally, the fourth level, "severe NPDR" includes ETDRS grades 53 and higher, carries with it the most threatening forecast for progression to PDR.

Table 1 – Summary of the retinopathy severity scales presented in ETDRS [27].

Grade	Severity level	Description
10	No DR	No abnormalities
20	Microaneurysm only	MA
35	Mild NPDR	SE, IRMA or RH or HE or SE
47	Moderate NPDR	HA/MA or IRMA
53	Severe NPDR	HA/MA or IRMA or VB
61	Mild PDR	FPD
71	High risk PDR	VH or PRH or VB
81	Advanced PDR	–

where HE: hard exudates, SE: soft exudates, IRMA: intraretinal microvascular abnormalities, IRH: intraretinal hemorrhage, VB: venous beading, PDR: proliferative DR, FPD: fibrous proliferations disc, VH: vitreous hemorrhages, PRH: preretinal hemorrhages.

Table 2 – International clinical DR disease severity scale [28].

Severity level	Findings observable with dilated ophthalmoscopy
No apparent retinopathy	No abnormalities
Mild NPDR	MAs only
Moderate NPDR	More than just MAs but less than severe NPDR
Severe NPDR	Any of the following: more than 20 IRH in each of 4 quadrants; definite VB in 2 + quadrants; prominent IRMA in 1 + quadrant; and no signs of PDR
PDR	One or more of the following: neovascularization, VH/PRH

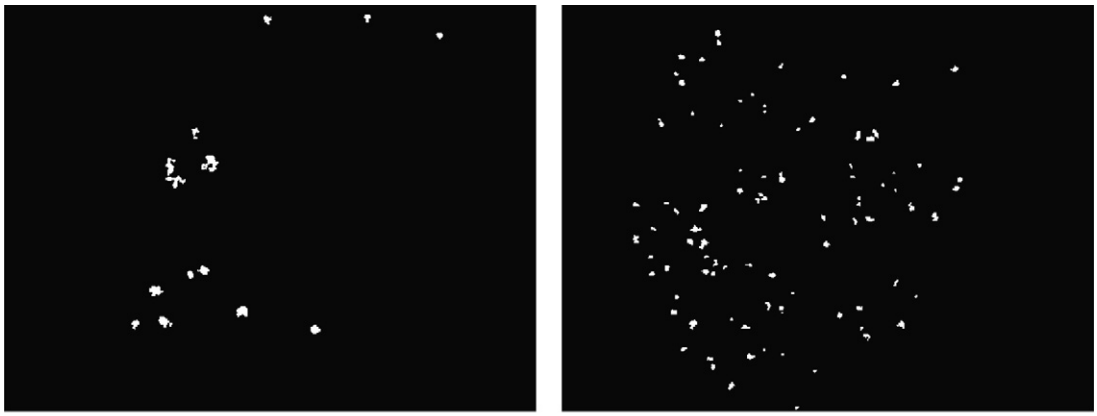

Fig. 10 – (a) Binary image which contains HAs, (b) binary images which contains MAs.

3. Results and discussion

The performance of the proposed algorithm was evaluated using a database of 98 low-resolution color images compressed by JPEG format. As mentioned earlier, the database comprises two sets of images with different sizes. The presence of MAs and HAs within the test images were as follows:

Set 1: In 62 images of size 480 × 640 pixels, the specialist manually marked the locations of 372 individual MAs as well as 217 HAs in individual images.

Set 2: In 36 images of size 576 × 768 pixels, the specialist manually marked the locations of 157 individual MAs as well as 112 HAs in individual images.

The proposed algorithm was tested on 38 images (normal (8), mild (13), moderate (12) and severe (5)) and trained on 60 images (normal (14), mild (23), moderate (16) and severe (7)). The sets of images used for training and testing are completely different. There is no overlapping between these two sets. A comparison between the results of the proposed segmentation algorithm against the manually marked images was done in order to measure the performance of the proposed classification algorithm. The performance evaluation was measured based on two statistical criteria, namely, sensitivity [29,30], specificity [29,30] and kappa coefficient [31], which can be calculated using Eqs. ((17)–(21)) respectively.

$$\text{Sensitivity} = \frac{TP}{TP + FN} \tag{17}$$

$$\text{Specificity} = \frac{TN}{TN + FP} \tag{18}$$

$$\text{kappa} = \frac{Pr(o) - Pr(e)}{1 - Pr(e)} \tag{19}$$

$$Pr(o) = \frac{(TP + TN)}{(TP + TN + FP + FN)} \tag{20}$$

$$Pr(e) = \frac{[(TP + FP) * (TP + FN)] + [(FN + TN) * (FP + TN)]}{(TP + TN + FP + FN)^2} \tag{21}$$

Table 3 – Performance of the proposed classification algorithm.

Spot lesion	Sensitivity (%)	Specificity (%)	Kappa (%)
MAs	84.31	93.63	68.98
HAs	87.53	95.08	74.91

where *TP*, *TN*, *FP*, and *FN* represent true positive, true negative, false positive, and false negative respectively. Table 3 presents the experimental results obtained by the proposed algorithm, which reveals that the algorithm yields promising results in terms of sensitivity and specificity even though only low-quality images were used as test images. It may be mentioned that the specificity values in Table 3 may not represent the true situation due to the fact that these values are calculated on pixel by pixel basis and the lesion regions in general occupy a relatively smaller portion of the image. The test images were classified into four groups by the specialist, as shown in Table 4. Based on the results given in Table 4, we have also determined the sensitivity and specificity values for the presence of diabetic retinopathy (mild, moderate and severe) versus no diabetic retinopathy and they are found to be 89.47% and 95.65% respectively. Besides the classification accuracy results, the proposed system yields a grading rate for the severity level with 90.81%, which indicates that 9 images out of 98 were incorrectly graded. It is expected that the proposed system will yield better results if it tested using high-quality images. Simulation was carried out to estimate the performance of the developed system and to enable the user to interact with the features of the system. Fig. 11 presents a

Table 4 – Performance of the proposed system compared to the grading of a specialist.

Group	No. of images graded by Specialist	No. of images graded by the proposed system
Normal	22	21
Mild	36	33
Moderate	28	25
Severe	12	10

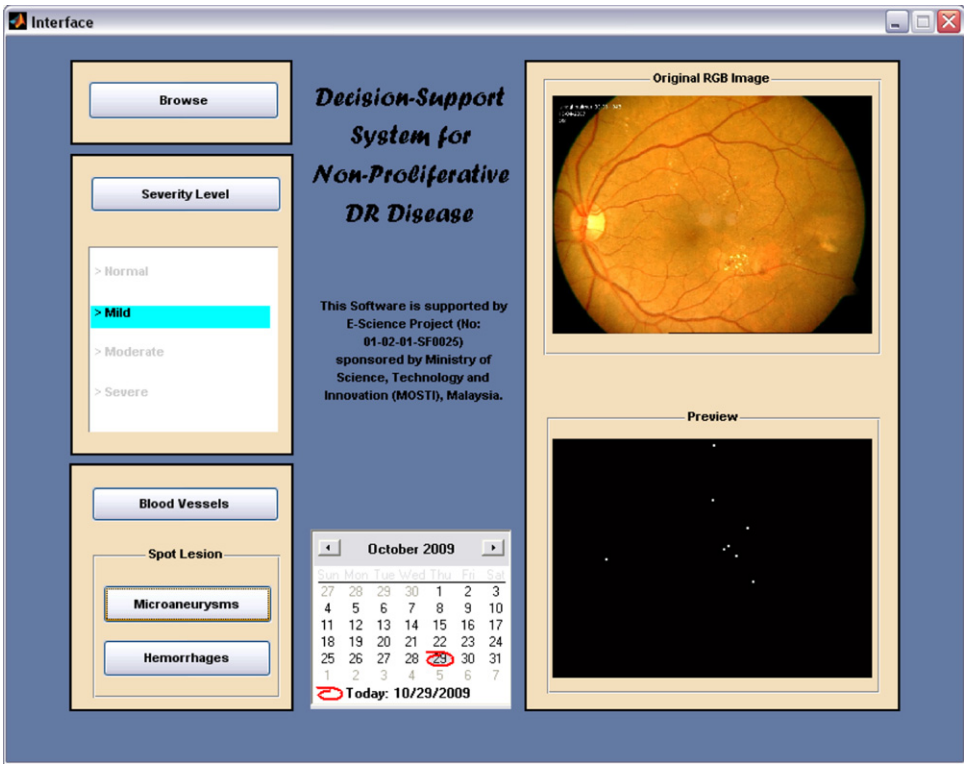

Fig. 11 – Simulation of the developed system.

graphic user interface (GUI) which has been designed using MATLAB v. 7.7. For extracting the blood vessels, the proposed system uses the algorithm reported in [32].

4. Conclusions

Algorithms for the extraction of microaneurysms and hemorrhages from fundus images have been presented. An automated decision-support system for DR disease has been designed based on these features. A user-friendly interface has also been presented. The severity level grading of DR has been performed based on the rules which have been reported in the International Clinical Diabetic Retinopathy Disease Severity Scale. The proposed algorithm extracts first the main components of the human retina, i.e. the optic disc, fovea, and tissue for easier segmentation. Then, an efficient algorithm based on h-maxima transformation and multilevel thresholding has been employed for dark spot segmentation. Suitable classification algorithm has also been proposed to classify the dark spots as MAs or HAs using some geometrical criteria. Finally, based on the number and location of MAs and HAs, the severity level has been graded into four scales, i.e. normal, mild, moderate, or severe. Experiments have been conducted using 98 low-quality color images to evaluate the performance of the developed system. A comparison between the results of the proposed system against the manually marked images has been done. The experimental results show that the proposed system can achieve 84.31% and 87.53% in terms of sensitivity for the detection of MAs and HAs respectively, and 93.63% and 95.08% in terms of specificity. Also, the proposed system achieved 68.98% and 74.91% values in terms of kappa coefficient for the detection of MAs and HAs respectively Based on the experimental results, it is clear that the developed system yields promising results even though only low-quality images have been used as test images. It is expected that the system would yield better results if it is tested using high-quality images.

Conflict of interest

No conflict of interest is involved in this paper.

REFERENCES

[1] R. Klein, B.E. Klein, S.C. Jensen, et al., The relation of socioeconomic factors to the incidence of early age-related maculopathy The Beaver Dam Eye Study, Am. J. Ophthalmol. 132 (2001) 128–131.
[2] S.C. Lee, E.T. Lee, R.M. Kingsley, Y. Wang, D. Russell, R. Klein, A. Warn, Comparison of diagnosis of early retinal lesions of diabetic retinopathy between a computer system and human experts, Arch. Ophthalmol. 119 (2001) 509–515.
[3] T. Walter, P. Massin, A. Erginay, R. Ordonez, C. Jeulin, J.C. Klein, Automatic detection of microaneurysms in color fundus images, Med. Image Anal. 11 (6) (2007) 555–566.
[4] A. Thomas, Chiulla, G. Annando, Amador, Bernard, Zinman, Diabetic retinupathy and diabetic mucdur edema: purhophysiology, screening, and novel therapies – review article, Diabetes Care (2003).

[5] S.J. Lee, C.A. McCarty, H.R. Taylor, J.E. Keeffe, Costs of mobile screening for diabetic retinopathy: a practical framework for rural populations, Aust. J. Rural Health 8 (2001) 186–192.
[6] H.R. Taylor, J.E. Keeffe, World blindness: a 21st century perspective, Brit. J. Ophthalmol. 85 (2001) 261–266.
[7] L. Streeter, M.J. Cree, Microaneurysm detection in colour fundus images, in: Image Vision Comput. New Zealand, Palmerston North, New Zealand, November, 2003, pp. 280–284.
[8] J.V.B. Soares, J.J.G. Leandro, R.M. Cesar Jr., H.F. Jelinek, M.J. Cree, Retinal vessel segmentation using the 2-D Gabor wavelet and supervised classification, IEEE Trans. Med. Imaging 25 (9) (2006) 1214–1222.
[9] Early Treatment Diabetic Retinopathy Study Research Group:, Grading diabetic retinopathy from stereoscopic color fundus photographs–an extension of the modified Airlie House classification: ETDRS report number 10, Ophthalmology 98 (1991) 786–806.
[10] G.E. Øien, P. Osnes, Diabetic retinopathy: automatic detection of early symptoms from retinal images, in: Proc. Norwegian Signal Processing, September, 1995, pp. 135–140.
[11] M.J. Cree, J.A. Olson, K.C. McHardy, P.F. Sharp, J.V. Forrester, A fully automated comparative microaneurysm digital detection system, Eye 11 (1997) 622–628.
[12] T. Spencer, J. Olson, K. McHardy, P. Sharp, J. Forrester, An imageprocessing strategy for the segmentation and quantification in fluorescein angiograms of the ocular fundus, Comput. Biomed. Res. 29 (1996) 284–302.
[13] A. Frame, P. Undrill, M. Cree, J. Olson, K. McHardy, P. Sharp, J. Forrester, A comparison of computer based classification methods applied to the detection of microaneurysms in ophthalmic fluorescein angiograms, Comput. Biol. Med. 28 (1998) 225–238.
[14] M. Niemeijer, B. van Ginneken, J. Staal, M.S.A. Suttorp-Schulten, M.D. Abràmoff, Automatic detection of red lesions in digital color fundus photographs, IEEE Trans. Med. Imaging 24 (5) (2005) 584–592.
[15] T. Walter, J.-C. Klein, Automatic detection of microaneurysms in color fundus images of the human retina by means of the bounding box closing, in: A. Colosimo, A. Giuliani, P. Sirabella (Eds.), Lect. Notes Comput. Sci. (LNCS) 2526 (2002) 210–220.
[16] Walter, T., 2003. Application de la Morphologie Mathématique au diagnostic de la Rétinopathie Diabétique à partir d'images couleur. Ph.D. Thesis, Centre of Mathematical Morphology, Paris School of Mines, September.
[17] T. Walter, P. Massin, A. Erginay, Ri. Ordonez, C. Jeulin, Jean-Claude Klein, Automatic detection of microaneurysms in color fundus images, Med. Image Anal. 11 (2007) 555–566.
[18] D. Gardner, T. Keating, A. Williamson, Elliot, Detection of diabetic retinopathy using neural network analysis of fundus images, Br. J. Ophthalmol. 80 (11) (1996) 937–948.
[19] C. Sinthanayothin, J.F. Boyce, T.H. Williamson, H.L. Cook, E. Mensah, S. Lal, D. Usher, Automated detection of diabetic retinopathy on digital fundus images, Diabetic Med. 19 (February (2)) (2002) 105–112.
[20] D. Usher, M. Dumskyj, M. Himaga, T. Williamson, S. Nussey, J. Boyce, Automated detection of diabetic retinopathy in digital retinal images: a tool for diabetic retinopathy screening, Diabetes Med. 21 (2004) 84–90.
[21] A.D. Fleming, S. Philip, K.A. Goatman, J.A. Olson, P.F. Sharp, Automated microaneurysm detection using local contrast normalization and local vessel detection, Trans. Med. Imaging 25 (9) (2006) 1223–1232.
[22] G. Quellec, M. Lamard, P.M. Josselin, G. Cazuguel, B. Cochener, C. Roux, Optimal wavelet transform for the detection of microaneurysms in retina photographs, EEE Trans. Med. Imaging 27 (9) (2008) 1230–1241.
[23] P. Soille, Morphological Image Analysis, 2nd ed., Springer, 2004, ISBN: 3540429883.
[24] R.C. Gonzalez, R.E. Woods, Digital Image Processing, 3rd ed., Prentice hall, 2008, ISBN: 013168728x.
[25] The MathWorks, Inc. (1984–2009). The MATLAB Package, [Online]. Available from: http://www.mathworks.com/.
[26] G. Yen Gary, Wen-Fung Leong, A sorting system for hierarchical grading of diabetic fundus images: a preliminary study, IEEE Trans. Inform. Technol. Biomed. 12 (1) (2008).
[27] Early Treatment Diabetic Retinopathy Study Research Group: Fundus photographic risk factors for progression of diabetic retinopathy. ETDRS Report Number 12. Ophthalmology 98 (1991) 823–833.
[28] C.P. Wilkinson, F.L. Ferris, R.E. Klein, et al., Proposed international clinical diabetic retinopathy and diabetic macular edema disease severity scales, Ophthalmology 110 (2003) 1677–1682.
[29] L. Costaridou, Medical Image Analysis Methods The Electrical Engineering and Applied Signal Processing Series, CRC Press, 2005, ISBN: 0-8493-2089-5.
[30] T. Athanasiou, A. Darzi, Evidence Synthesis in Healthcare: A Practical Handbook for Clinicians, Springer, 2011, ISBN: 978-0-85729-175-2.
[31] J. Cohen, A coefficient of agreement for nominal scales, Educ. Psychol. Measur. 20 (1) (1960) 37–46.
[32] M.D. Saleh, C. Eswaran, A. Mueen, An automated blood vessel segmentation algorithm using histogram equalization and automatic threshold selection, J. Digit. Imaging 24 (4) (2011) 564–572.